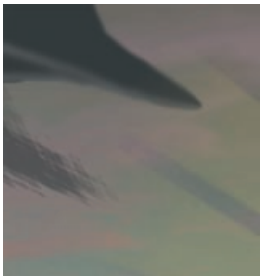

A Site-Specific Model of Radar Terrain Backscatter and Shadowing

Christopher C. Lin and J. Patrick Reilly

A site-specific approach is presented to characterize terrain and target visibility and terrain clutter as seen by a shipboard radar in a coastal environment. The method takes into account the location of the ship, the particular terrain topography, the radar parameters, and the propagation effect. The method incorporates atmospheric refractive index conditions surrounding the radar, an optical ray-trace model, an electromagnetic parabolic equation model, a database of terrain elevations, and a clutter model. The model can simulate illuminated and shadowed regions of both surface clutter and elevated targets. Simulated clutter results are shown to compare favorably with clutter data measured at S-band, X-band, and Ku-band. This correspondence is evident in geo-graphic patterns and statistical distributions of clutter on directly illuminated terrain surfaces.
(Keywords: Littoral model, Radar clutter, Radar modeling, Radar propagation, Terrain effects.)

INTRODUCTION

A shipboard radar in a coastal region is subject to complications not encountered in the open ocean. These complications include terrain shadowing of air targets over land and clutter returns from terrain. Terrain shadowing occurs in geographic patterns dictated by specific terrain contours, resulting in regions of attenuated radar signal strength that can compromise detection and tracking. Terrain clutter can obscure a target's signal, even when it is not in shadow as well as the clutter at a range distant from the target. Both terrain shadowing and clutter are significantly affected by the characteristics of electromagnetic propagation, which can be complicated in the coastal region.

Existing models for land clutter are typically empirical. For instance, tables and empirical formulas are available in which reflectivity for generic types of terrain is related to various radar parameters.[1–6] Typically, some statistical measure is given, such as mean or median reflectivity (σ_0), often along with parameters of some statistical model. Such models suffer from a

number of deficiencies, including the inability to account for site-specific terrain features, geographic patterns of clutter, propagation conditions, or target shadowing. Other researchers have developed models that account for site-specific terrain features,[7,8] but these models fail to account for arbitrary propagation conditions and do not represent target shadowing.

The model described here overcomes these deficiencies. Features of the model include three-dimensional refractive index specifications, an optical ray-trace model, an electromagnetic parabolic equation model, and a database of terrain elevations called DTED (Digital Terrain Elevation Data), which is published by the Defense Mapping Agency. The database provides terrain elevations on a 100-m grid for much of the Earth's land mass. The model can accept refractivity inputs that vary in three dimensions if such detailed data are available. Alternatively, a single profile of refractive index versus altitude may be used to represent a uniformly stratified atmosphere, i.e., a condition in which the refractive index versus altitude is constant over the area covered by radar.

The terrain effects model is currently configured with various levels of complexity and fidelity. A Terrain Visibility Routine (TEVIR) calculates regions of the terrain or of the air space above the terrain that are subject to direct illumination by the radar. TEVIR-I performs such calculations for an atmosphere characterized by a linear, nonducting refractivity profile, of which the standard atmosphere is a specific case. TEVIR-I performs calculations using straight-line ray trajectories over a round Earth having an equivalent Earth radius dictated by the refractivity slope. For the standard atmosphere, the equivalent Earth radius is a factor of 1.33 greater than the true Earth radius. TEVIR-II can use arbitrary refractivity profiles, including profiles that vary in both range and azimuth from the radar location. TEVIR-II makes use of an optical ray-trace routine. A third variant called the RADSCAT (radar scattering) model determines propagation effects using an electromagnetic parabolic equation method. This method involves a full-forward-wave calculation of the electromagnetic field. The parabolic equation is numerically solved in RADSCAT by the Fourier split-step method, using the computer model called TEMPER developed at the Applied Physics Laboratory.[9,10] The RADSCAT model with TEMPER provides numerical calculations of the propagation factor and accounts for radar refraction, multipath, and diffraction. The more complex RADSCAT model is used to calculate quantitative radar clutter data. Like TEVIR-II, RADSCAT can accept three-dimensional refractivity inputs.

VISIBILITY MAPS

General Considerations

We determine terrain visibility by one of two methods: an optical ray-trace program or an electromagnetic parabolic equation model (TEMPER). In both methods, electromagnetic energy is assumed to be reflected from water surfaces but absorbed by terrain.

The optical ray-trace (geometric optics) method integrates propagation differential equations along a ray trajectory. In the ray-trace method, rays are launched at closely spaced elevation angles. Typically, both positive and negative angles are included; the negative ones are reflected from the water surface. The range of angles needed to simulate radar visibility depends on the beamwidth of the radar, the maximum altitude of terrain peaks, and the range of the terrain peaks to the radar. In a typical simulation of a shipboard radar, maximum ray angles of ±2° are usually sufficient to completely account for all rays that intersect the terrain. The trajectory of each ray is calculated for a particular refractivity profile. Once a ray encounters a land surface, that surface is considered illuminated for subsequent ranges along an equal azimuth slice until the terrain slope becomes negative. For ranges beyond the negative terrain slope, the terrain is considered to be in shadow until another ray intersects the terrain surface. By repeated application of this algorithm, one can identify directly illuminated regions along a radial slice; with slices along various azimuths, one can identify directly illuminated areas of terrain. The accuracy of the resulting plot improves as we increase the density of rays within the elevation launch angles and as we increase the density of azimuth slices. For a typical application, we obtain satisfactory results with elevation ray spacing of about 0.02° and azimuth spacing of about 0.5°.

The number of ray calculations can become quite large. For example, using ±2° elevation coverage with 0.02° spacing and 90° azimuth coverage with 0.5° spacing, there are 36,000 ray trajectories to be computed if the refractivity profiles are unique along each azimuth slice. For a uniformly stratified atmosphere, however, the number of calculated rays need be only 200 by using the same set of trajectories at each azimuth angle.

One can often evaluate the potential severity of terrain clutter problems by examining a terrain visibility map showing the regions of terrain that are directly illuminated (i.e., not in shadow). Often the distribution and extent of visible terrain are sufficient to estimate the probable impact of clutter. In such cases, a ray-trace solution obtained by TEVIR-I and -II may be sufficient for a qualitative radar performance evaluation.

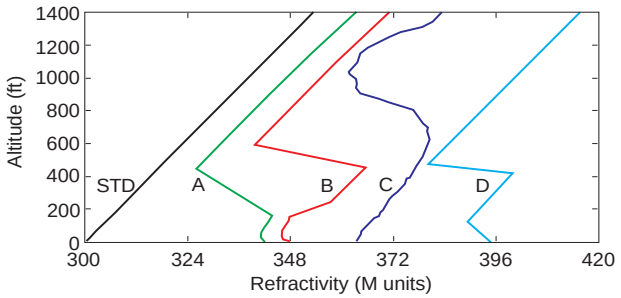

Figure 1. Measured refractivity profiles off the coast of California (A, B, and C) and in the Arabian Gulf (D). A and B were measured by the Pacific Missile Test Center in June 1990; C was measured by APL in the summer of 1992; D was measured by APL in June 1995. (STD = standard atmosphere profile.)

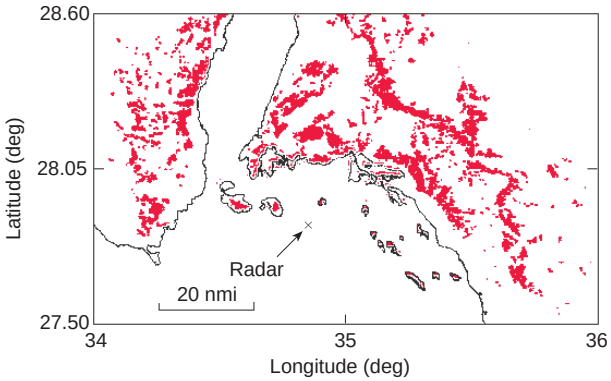

Figure 3. Terrain visibility diagram determined by the ray-trace method for a radar located in the Red Sea with standard atmosphere propagation.

In this article, we will examine propagation effects using the refractivity profiles shown in Fig. 1. Profiles A and B were measured by the Pacific Missile Test Center off the coast of California over a 3-day period in June 1990. Strong surface-based ducts were persistent during this period. Profile C was measured off the coast of California by APL personnel during the summer of 1992. Surface-based duct heights of 500, 600, and 1000 ft apply to profiles A, B, and C, respectively. The profiles include evaporation ducts at the surface. Profile D was measured in the Arabian Gulf in June 1995. This profile includes an 461-m elevated duct and a 38-m surface-based duct. An additional profile representative of a standard atmosphere is also shown in Fig. 1. When using the profiles of Fig. 1, we retain the evaporation duct for propagation over the sea. However, we assume that the evaporation duct does not exist over land. For overland applications, we delete the evaporation duct and extrapolate the refractivity profile above that duct to the surface. The refractivity profiles shown here have been constructed from temperature, pressure, and humidity constituents, using relationships given in Reilly et al.[11] The evaporation duct profile has been constructed using a surface boundary layer model with a neutrally buoyant condition.[12]

Terrain Visibility–Ray-Trace Solutions for Stratified Atmosphere

Figure 2 is an example of a DTED terrain profile and ray trajectories with standard atmosphere propagation. The highlighted areas are those in direct illumination, according to the procedure described under "General Considerations." Figure 3 is a terrain visibility diagram for a radar located in the Red Sea with standard atmosphere propagation. The region shown is characterized as "high-relief terrain," having terrain peaks of 8200 ft. Figure 4 is a ray diagram for a refractivity profile involving a uniformly stratified, 600-ft surface-based duct (identified as profile 6 in Ref. 11). Figure 5 shows the same area as in Fig. 3, but with a 600-ft surface-based duct.

By comparing Figs. 3 and 5, one sees significant differences in the patterns of visible terrain under standard atmosphere and ducting conditions. Clearly, much more terrain is directly illuminated with the 600-ft duct

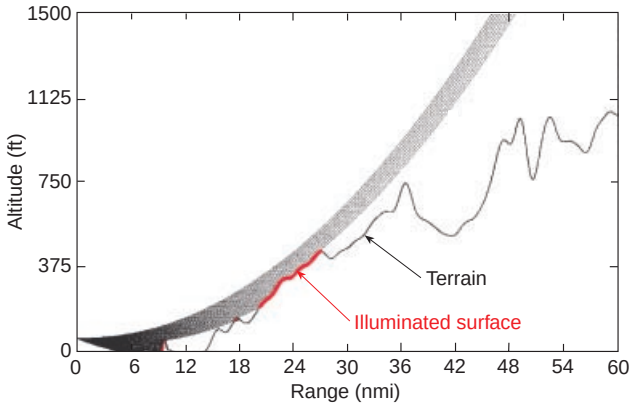

Figure 2. Terrain and ray-trace profile with standard atmosphere propagation.

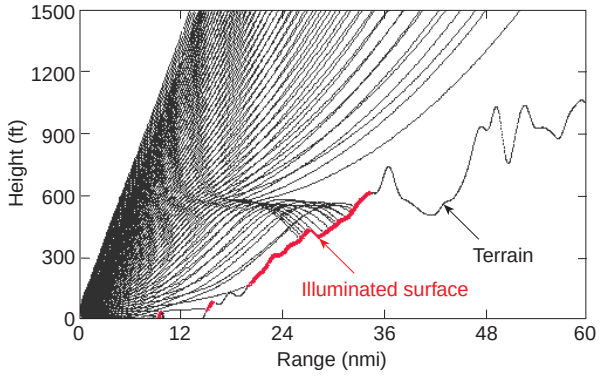

Figure 4. Terrain and ray-trace profile with a 600-ft surface-based duct.

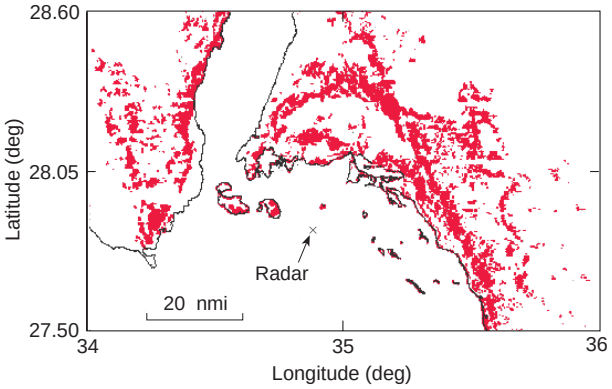

Figure 5. Terrain visibility diagram determined by the ray-trace method for a radar located in the Red Sea with a 600-ft surface-based duct and uniformly stratified atmosphere.

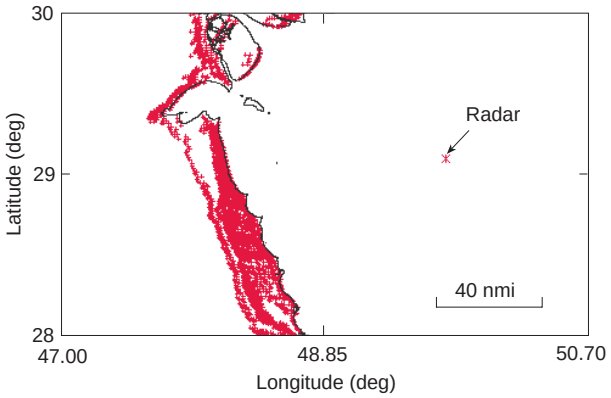

Figure 7. Terrain visibility diagram for operation near Saudi Arabia, 1000-ft surface-based duct. The radar was 70 nmi from the coast.

than with the standard atmosphere. However, the maximum extent of the clutter is similar in the two cases. The increased density of illuminated terrain under ducting may be explained by the downward refraction of radar energy, which illuminates features that might otherwise be hidden, as suggested in Fig. 4. The terrain at great distances is illuminated primarily by rays that escape the duct and intersect high-altitude terrain features. For that reason, there is not a large difference in the maximum extent of visible terrain in the two cases shown here.

Figures 6 through 9 illustrate terrain visibility with propagation via a 1000-ft surface-based duct (profile C of Fig. 1) near the coast of Saudi Arabia. In these examples, the terrain is characterized as low-to-medium relief, with peaks of about 1000 ft. With the radar situated 70 nmi from the coast (Fig. 7), the directly illuminated terrain is confined to a narrow band about 20 nmi wide along the coast. However, by moving the radar to a location that is 25 nmi more distant (Fig. 8), the directly illuminated terrain extends to about 75 nmi from the coast (Fig. 9)—a significant increase relative to Fig. 7. The extended visibility in Fig. 9 occurs because of the opportunity for reflected paths from the ocean surface to intersect distant terrain via the surface-based duct model as indicated in Fig. 8.

Modification of Refractivity Profiles by Terrain

The atmospheric constituents that govern refractivity are temperature, pressure, and humidity—parameters that are subjected to terrain influences. Consequently, a realistic atmospheric model would include terrain-related modifications to the refractivity profiles, in contrast to the simple stratified atmospheric assumptions used in the previous examples. To illustrate the ability to represent terrain influences, we simulated an adiabatic sea breeze (ASB) model in which a sea breeze transports the air mass from the sea to the land.[11] We assumed that as the air mass is raised in altitude, it undergoes adiabatic expansion (i.e., heat is neither added nor subtracted). We assumed knowledge of temperature, pressure, and humidity versus height over the sea, and that the temperature, pressure, and humidity constituents are transformed via an adiabatic process as the air mass is transported over the land. As the air mass

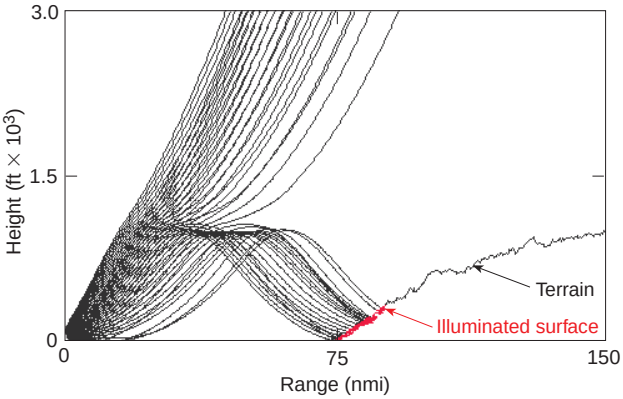

Figure 6. Ray diagram for operation near Saudi Arabia with a 1000-ft surface-based duct. The radar was 70 nmi from the coast.

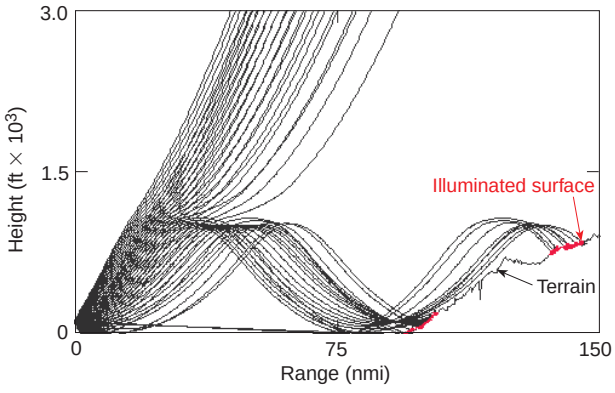

Figure 8. Ray diagram for operation near Saudi Arabia with a 1000-ft surface-based duct.The radar was 95 nmi from the coast.

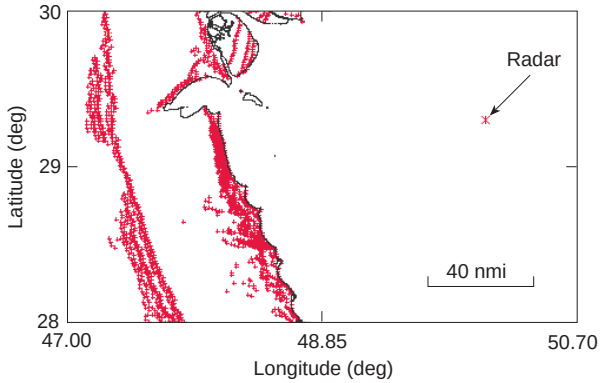

Figure 9. Terrain visibility diagram for operation near Saudi Arabia, 1000-ft surface-based duct. The radar was 95 nmi from the coast.

moves inland, we calculated new constituent profiles at range increments ΔR. We then interpolated the constituents between calculated profiles using a linear interpolation procedure. In Fig. 5 of Ref. 11, the ASB model was applied to profile A of Fig. 1 with a ship position in the Red Sea as in Fig. 5. When the visibility diagrams generated by the ASB and stratified atmosphere models are compared, one can observe differences in specific regions. However, the overall density and range extent of illuminated terrain are similar in the two cases considered. For other classes of terrain relief, however, one might expect greater differences between a stratified atmosphere and an ASB process.

It is not our intention to represent the ASB model as a realistic case, but rather to demonstrate the ability of our visibility and clutter models to incorporate the interaction of terrain and atmospheric processes. Although the ASB process introduces additional complexities into the refractivity model, it is nevertheless a simplification of the physical processes present in coastal meteorology. We have ignored a number of phenomena likely to be important, such as boundary layer phenomena, heat inputs from the terrain, and more complex air movement patterns.

Visibility of Air Targets

Besides the clutter processes discussed here, terrain shadowing can limit the ability of the radar to detect and track overland targets. It is often useful to evaluate target shadowing limitations using a target visibility diagram as illustrated in Fig. 10. This example applies to air targets over former Yugoslavia, for a ship position approximately 25 nmi off the coast; the calculated visibility assumed a standard atmosphere. It is assumed that the air target flies at a constant height above the terrain. The shaded regions indicate where an air target at several different heights would be directly illuminated by the radar. The coded regions should be interpreted as being cumulative, e.g., the colored region applying to 10,000 ft also includes the regions for lower- altitude targets. This visibility diagram was produced by calculating ray trajectories and applying a visibility algorithm similar to the procedure used to determine terrain visibility as described under "General Considerations."

Application of Electromagnetic Propagation Routine

The ray-trace methods discussed earlier provide relatively fast qualitative solutions. The TEMPER program provides more detailed quantitative calculations of the total electromagnetic field using the Fourier split-step method.[9,10] Inputs to TEMPER include the radar frequency, polarization, antenna elevation beam pattern, antenna elevation pointing angle, and refractivity profiles (index of refraction versus height). The refractivity profiles may vary with range if such detailed information is available. In our applications, the relevant output of TEMPER is the one-way or two-way propagation factor F^2 or F^4, where $F = |E/E_o|$, E_o is the free-space field, and E is the field under the assumed conditions. We have adapted TEMPER to simulate a lower terrain boundary by setting the calculated field to zero at and below the terrain boundary at each range increment.[13] The first nonzero field value above the terrain surface is identified with field strength incident

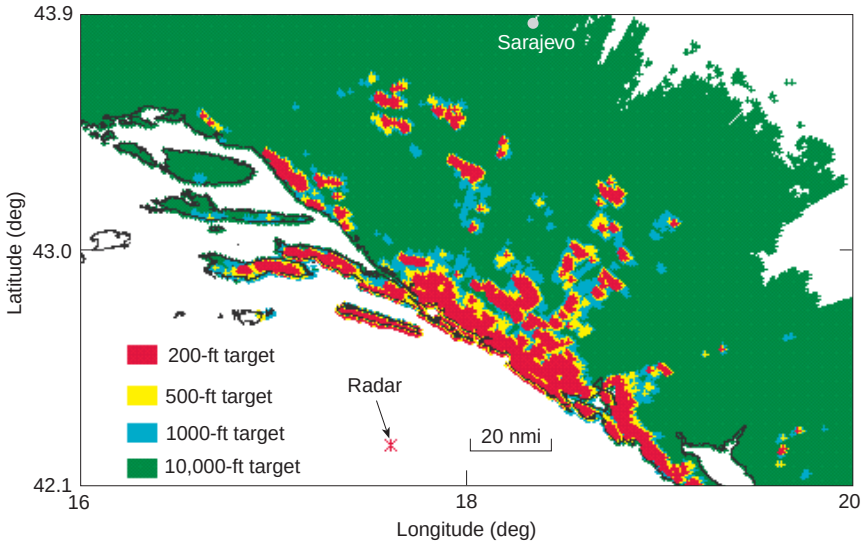

Figure 10. Visibility of air targets for a ship position off the coast of former Yugoslavia, with standard atmosphere propagation.

on the surface at that range. This procedure essentially represents the terrain as a series of knife edges, which behaves as an approximation to a perfectly absorbing boundary. With this method, the TEMPER calculation will be unique for each azimuth slice.

Figure 11 illustrates a TEMPER solution using a particular terrain slice as a lower boundary; F^2 has been coded on a color scale. The solution includes diffraction energy in regions that would be considered in shadow according to the ray-trace algorithm. This example was generated using profile B of Fig. 1 to specify refractivity—the same profile used in the ray diagram of Fig. 4. Other relevant parameters for Fig. 11 are S-band, vertical polarization, 1.5° beamwidth, and 0° antenna pointing angle.

By applying the TEMPER program to each azimuth slice, a terrain visibility map may be obtained. Although the TEMPER method does not explicitly determine shadowed terrain, one can obtain a terrain visibility map by applying a threshold to F^2. In Ref. 13, a visibility map was generated by applying a threshold of –6 dB to F^2. By comparing that visibility diagram with the one determined with the ray method (Fig. 5), one sees very little difference.

Terrain Boundary Assumptions

Both ray-trace and TEMPER methods make use of perfectly absorbing boundaries. However, the propagation models have the capability to include reflecting boundaries. For the ray method, one might calculate a reflected path after a ray encounters the terrain, taking into account the terrain slope in determining the reflected launch angle. For TEMPER, one might consider using a finite impedance lower boundary, such as has been studied elsewhere.[14,15]

Not only is our implementation of an absorbing boundary much simpler than alternatives using reflecting boundaries, but one can advance arguments for preferring an absorbing boundary. One argument is that reflected rays are unlikely to return energy to the surface at a more distant range. In most cases of practical interest, rays launched at more than 1° penetrate most practical ducts and are therefore not refracted back to the surface. Therefore, terrain slopes of more than 1° would not return reflected energy to more distant surface locations. Second, energy will tend to be diffusely reflected because realistic terrain is typically very rough compared with radar wavelengths. Consequently, a specular reflection or smooth surface calculation is usually unrepresentative. Thirdly, absorption at the boundary because of finite impedance will further diminish the reflected energy.

To adequately assess the impact of terrain boundary assumptions, more modeling efforts are required. Work continues at APL to develop finite impedance boundary applications that we will eventually apply to our terrain effects models.

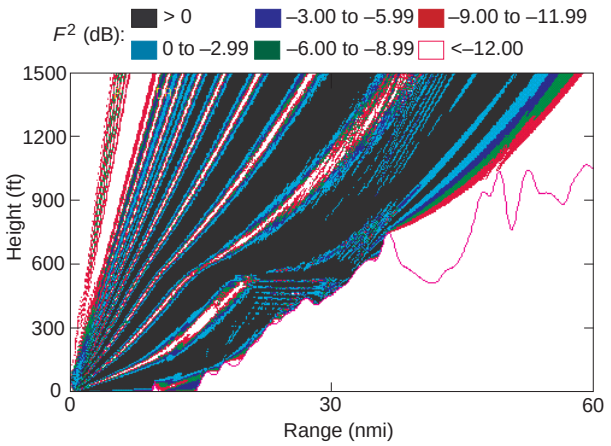

Figure 11. Illustration of terrain and propagation factor profile with a 600-ft surface-based duct. F^2 = one-way propagation factor.

CLUTTER CALCULATIONS

General Relationships

Clutter magnitude depends on both radar system and terrain parameters. Radar system parameters include transmitter power, frequency, antenna gain, and resolution size (both range and azimuth). Terrain parameters comprise type, roughness, reflectivity, and location relative to the radar. Clutter power can be expressed by

$$P_c = \frac{P_t G^2 \lambda^2 \sigma_0 F^4 A_c}{(4\pi)^3 R^4 L}, \qquad (1)$$

where P_c is returned clutter power, P_t is transmitted power, G is antenna gain, λ is radar wavelength, σ_0 is the average clutter reflectivity of a radar cell, F^4 is the two-way propagation factor, A_c is the area of an illuminated cell, R is the range to the clutter cell, and L represents various system losses.

Using the "constant-gamma" model, the clutter reflectivity is defined as

$$\sigma_0 = \frac{1}{n}\sum_i^n \sigma_{0i} = \frac{1}{n}\sum_i^n \gamma \sin\psi_i, \qquad (2)$$

where n is the number of DTED facets (defined in Ref. 11) within a radar cell, σ_{0i} (m^2/m^2) is the reflectivity of the ith facet, ψ_i is the grazing angle at the ith facet, and γ is the normalized reflectivity (m^2/m^2), which is

predefined and depends on the radar frequency and the type of terrain. We use the following frequency relationship in our model:

$$\gamma = \gamma_r \left(\frac{f}{f_r} \right)^k , \qquad (3)$$

where γ_r is a reference value applicable to a particular radar frequency f_r; according to Ref. 1, we use the frequency scaling factor $k = 0.5$. Whereas some data suggest that γ and k vary with both terrain relief and cultural development,[1,7] we currently use the same values for both high- and low-relief terrain, namely, $\gamma_r = 0.17$ at $f_r = 3.0$ GHz, and $k = 0.5$. The γ_r value has been increased relative to our previous estimates[12,13] to conform with the measurements presented in the succeeding section. We have not varied γ_r with terrain relief, reasoning that terrain relief factors due to large-scale shadowing may be adequately accounted for in our DTED-based method. We recognize, however, that the specification of γ_r for our model as a function of terrain type and frequency requires further investigation and clarification. In addition, grazing angle and radar frequency relationships are discussed further in the following section.

Generally one characterizes clutter in terms of the reflectivity parameter σ_0, which is expressed as a unitless quantity (m^2/m^2); σ_0 is usually determined by measuring returned clutter power and solving for σ_0 using Eq. 1. Since one typically lacks detailed knowledge of the propagation factor at the clutter source, it is customary to assume $F^4 = 1$ in this calculation. Recognizing the difficulty of separating reflectivity and propagation factor, we will characterize clutter reflectivity in terms of the combined parameter $\sigma_0 F^4$.

Parametric Variations

Many clutter models assume that the backscatter coefficient σ_0 increases with increasing grazing angle,[1–5] a trend in accordance with rough surface scattering theory.[16–18] Others have proposed a relationship based on depression angle of the radar antenna pattern rather than on grazing angle of the incident energy.[6,7] According to depression angle advocates,[7] the backscatter from terrain is dominated by processes involving vertically oriented features (e.g., trees, cultural features) and associated "microshadowing," rather than the rough surface mechanisms of theoretical models, and that general rough surface theory does not apply to most terrain. There are difficulties in defining appropriate angles in either view. Both depression and incidence angles are affected by atmospheric refractivity properties, and grazing angles are further affected by the fine structure of terrain slopes. In general, such details may not be accurately known.

Our current model uses a grazing angle relationship according to Eq. 2, where the grazing angle is defined by the slope of a ray from the ray-trace method and the terrain slope of a directly illuminated DTED cell. For shadowed regions, the grazing angle is approximated using the incidence angle of the previous ray and the local terrain slope. If the grazing angle in the shadow zone is negative (i.e., negative terrain slope exceeds ray inclination), we replace ψ_i with a minimum value in Eq. 2; this approximation is required to account for finite scattering due to surface roughness. In this article, the DTED terrain slope is determined as the slope along a two-dimensional slice. A more accurate definition of terrain slope would consider the three-dimensional slope of terrain. However, the error in backscatter coefficients by using a more simply determined two-dimensional slope is not excessive.[11]

Clutter reflectivity is often characterized using the parameter γ of Eqs. 2 and 3; γ is usually determined experimentally and may be separately specified for various terrain relief and cultural development classifications.[1] Past descriptions of γ can be only an initial guide for our applications for two reasons. First, most experimental data on γ apply to average reflectivity over an entire radar resolution cell, whereas in our applications, we apply γ to smaller DTED cells within a radar resolution cell. As a result, we would expect the appropriate γ value in our model to be different from the larger scale value determined in previous studies. Second, previous descriptions of γ include only generic classifications of terrain, whereas in our model the terrain slopes and shadowing features are separately determined for every DTED cell. Consequently, we hypothesize that aspects of terrain roughness might be accounted for in a DTED-based approach using DTED terrain slopes, and the same value of γ might apply to various terrain relief classifications. This hypothesis will have to be examined in future experimental studies of the sort presented in the "Experimental Verification" section of this article.

As discussed in that section, our experimental data are best fit using $\gamma = 0.17$ at S-band and 0.20 at Ku-band. The experimental value at Ku-band exceeds that at S-band by only 0.7 dB, whereas the difference expected from Eq. 3 is 3.25 dB. It will be necessary to conduct additional measurements before we can determine the experimental error in the estimate of γ or can confidently specify γ for other radar frequencies and terrain types. Hence, when making predictions of clutter strength, we use Eq. 3 with $k = 0.5$.

Example Calculation of Radar Clutter

Figure 12 shows the results of the RADSCAT land clutter model for an S-band radar with the following parameters: 0° antenna elevation pointing angle, 1.5° beamwidth (both azimuth and elevation), horizontal polarization, 1-μs pulse width, and 62-ft antenna height. Figure 12a is the land profile at a particular radar azimuth. The highlighted surfaces are visible by radar, as determined by the ray-trace program. Note that the land profile presents only one slice of terrain. Within the azimuthal radar beamwidth, the terrain profiles could vary, especially at large distances from the radar. In our simulations, we generally compute at least two slices within each beamwidth. Figure 12b shows the one-way propagation factor F^2 computed by TEMPER with profile B from Fig. 1. Figure 12c shows $\sigma_0 F^4$ versus range. When σ_0 is computed by Eq. 2, the incident angle within a shadowed region is assumed to be the same as that of the last ray on the illuminated surface. Figure 12d depicts the returned clutter power calculated by

$$P_c = k\frac{\sigma_0 F^4 A_c}{R^4}. \qquad (4)$$

For convenience of calculation and plotting, we evaluate Eq. 4 using $k = 10^{10}$, determined with A_c having units of square nautical miles, and R having units of nautical miles. Figure 12d shows clutter power not only from directly illuminated terrain but also from shadowed regions due to diffraction.

One can construct a clutter map by repeating the calculations shown in Fig. 12 at incremental azimuth angles. Figure 13 is a radar clutter map ($\sigma_0 F^4$); the assumed propagation condition and radar location are those used in the visibility diagram of Fig. 5. The radar parameters in this example are S-band, 3° beamwidth, 0° elevation pointing angle, 2-μs pulse width, and 62-ft antenna height. In Fig. 13, the magnitude of $\sigma_0 F^4$ is indicated with a gray scale. The azimuth increment is 0.5°.

Statistical Representation

The Weibull distribution is often used to represent the statistical distribution of terrain clutter. Statistical representations of terrain clutter can, however, be ambiguous and lead to misinterpretation. Therefore, one must

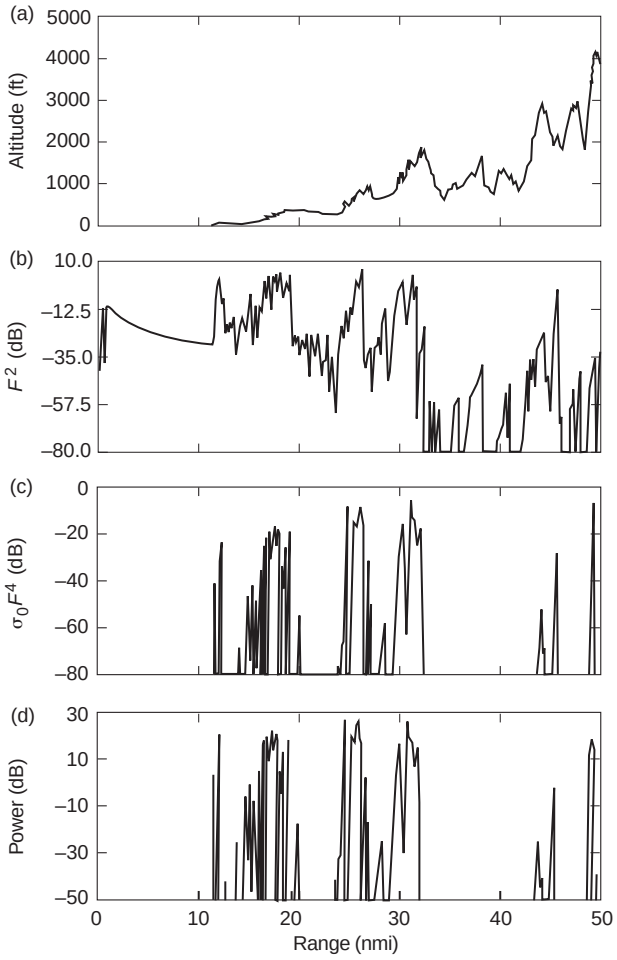

Figure 12. Land clutter return of an S-band radar simulation under a heavy surface duct propagation condition. (a) Terrain profile at radar beam center; (b) one-way propagation factor (F^2); (c) radar clutter reflectivity ($\sigma_0 F^4$); (d) returned clutter power.

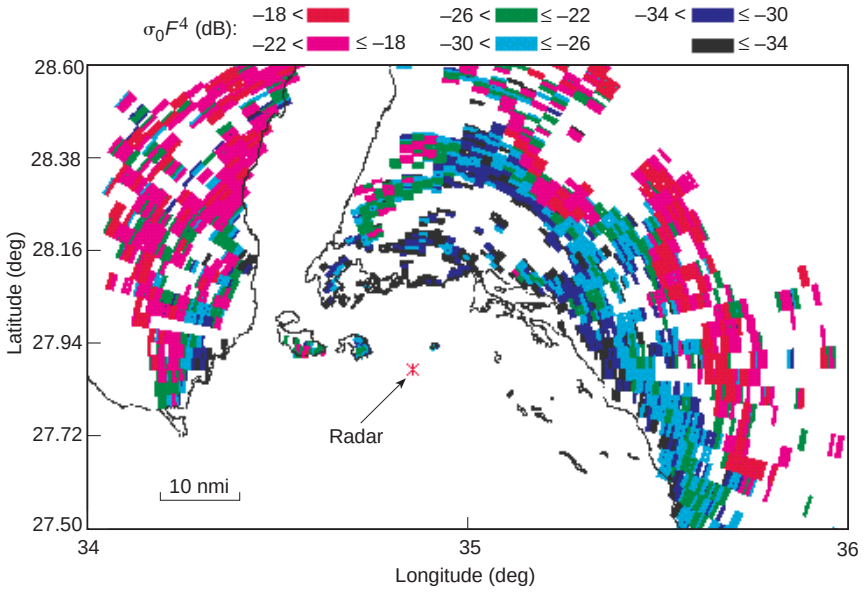

Figure13. Radar clutter map ($\sigma_0 F^4$).

be circumspect in interpreting and applying statistical clutter models. A major reason for this ambiguity is the influence of the minimum threshold used in the statistical database, a parameter that is usually unstated in descriptions of experimental clutter data.

The selection of a lower limit in simulated data is arbitrary. Since the model has no absolute lower limit on $\sigma_0 F^4$, one could set a lower threshold to exclude weak clutter data. The effect would be to alter the statistical parameters of the resulting database. As a practical matter, a similar issue will be present with measured data. Radar measurements will be limited to clutter cells that exceed a minimum signal-to-noise ratio (SNR), and this minimum will be a function of the sensitivity of the radar, including transmitter power, antenna gain, noise figure, and other parameters. To illustrate this point, imagine that clutter measurements are made by two radars that differ in sensitivity but are identical in all other respects. If we set a threshold at some multiple of the SNR, the more sensitive radar would include more data points with small values of $\sigma_0 F^4$ and would have a smaller average $\sigma_0 F^4$.

We illustrate this situation in Figs. 14 and 15, which give simulated cumulative count distributions of $\sigma_0 F^4$ for low- and high-relief terrain, respectively, including the frequency scaling law of Eq. 3. Figures 14 and 15 were determined with Eq. 3 and a hypothetical value of $\gamma = 0.05$ at S-band. Three radars are represented, differing only in frequency. The high-relief terrain (Fig. 15) applies to the Red Sea area with the radar looking eastward toward mountainous terrain in the azimuth sector 50–60° and a maximum range of 60 nmi. For low-relief terrain (Fig. 14), the radar is situated in the Arabian Gulf 10 nmi from the coast at 29.1° latitude and 48.3° longitude. The observed region covers the low-relief terrain of Kuwait and Saudi Arabia in the sector 260–270°, with a maximum range of 60 nmi. The simulated data include shadowed terrain illuminated through diffraction and do not have an absolute minimum value. Because of enhanced diffraction at longer wavelengths, small values of clutter are enhanced as the frequency band is lowered. However, the reverse is true at large values of $\sigma_0 F^4$, where clutter is enhanced as frequency is increased because of the scaling law given in Eq. 3.

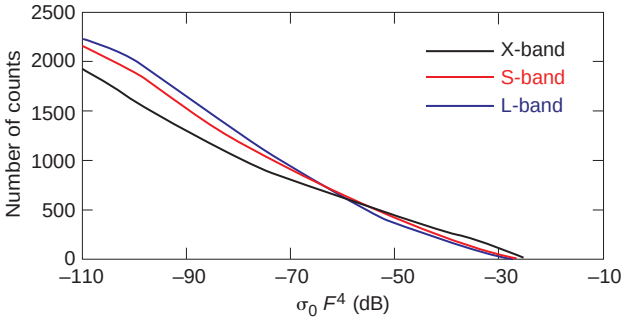

Figure 14. Cumulative distribution of radar clutter reflectivity ($\sigma_0 F^4$) in low-relief terrain.

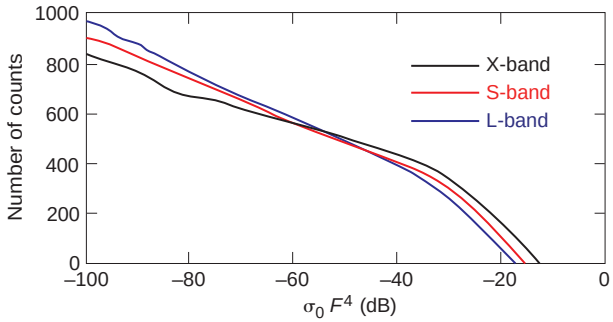

Figure 15. Cumulative distribution of radar clutter reflectivity ($\sigma_0 F^4$) in high-relief terrain.

Table 1 summarizes the averages of $\sigma_0 F^4$ and number of cells (N) exceeding the threshold when various thresholds are applied to the data of Figs. 14 and 15. From these data, one might infer that $\sigma_0 F^4$ has a frequency scaling law that depends both on threshold and terrain relief. A terrain relief dependency was also indicated in the measurements of Billingsley,[7] who found $\sigma_0 F^4$ to increase with increasing radar frequency in low-relief farmland but to decrease with increasing radar frequency in high-relief mountainous terrain.

In comparing simulation results with measurements, it is important to understand the difference in statistical properties of simulated and measured data. Whereas the model provides statistical expectations, i.e., statistical

Table 1. Statistics of radar clutter reflectivity ($\sigma_0 F^4$) with variation of threshold and radar frequency (1.5° beamwidth, 1-μs pulse width, 62-ft antenna height).

	L-band		S-band		X-band	
Threshold (dB)	Mean (dB)	N	Mean (dB)	N	Mean (dB)	N
High-relief terrain						
40	–34.3	568	–32.0	551	–29.3	549
30	–37.9	647	–36.4	641	–32.5	608
20	–42.3	739	–40.5	721	–35.7	660
10	–47.3	843	–44.8	804	–40.3	730
0	–50.6	912	–48.5	872	–45.8	817
–10	–53.0	963	–51.6	929	–49.5	875
Low-relief terrain						
40	–42.0	418	–41.8	462	–39.1	483
30	–48.3	683	–46.5	631	–43.1	627
20	–53.9	971	–52.2	908	–47.7	768
10	–59.7	1294	–57.9	1177	–54.0	992
0	–66.1	1684	–65.0	1549	–61.5	1286
–10	–70.7	1980	–70.7	1889	–70.0	1678

Note: Threshold refers to clutter-to-noise ratio for a hypothetical radar system. N = number of cells.

averages of reflectivity from individual radar cells, actual measurements include statistical fluctuations about these averages. The simulation results can be said to belong to a simple statistical distribution, whereas measurements will follow a compound distribution (see Fig. 23, which is discussed later).

EXPERIMENTAL VERIFICATION

Data Collection and Processing

Terrain clutter measurements were collected by a shipboard radar equipped with a coherent data collector (CDC), which has a 40-dB dynamic range. To increase the dynamic range, it was necessary to collect data with a series of attenuation as was done with S-band data. Data were collected near the west coast of the United States and near the Arabian Gulf in 1993 and 1995, respectively. The measured areas of the west coast of the United States are mountainous high-relief terrain; the measured areas of the Arabian Gulf have both mountainous high-relief and desert low-relief terrain. The terrain of both regions has a variety of features, including deserts, forests, vegetated land, urban areas, and rural areas. The tests did not include absolute calibration of the radar power. In relating radar measurements to absolute reflectivity, we relied on specified radar parameters.

Terrain clutter measurements were collected near the coast of southern California and northern Washington in May and June 1993. In this article, we present the data of southern California only. Pertinent radar parameters are S-band, horizontal polarization, 1.6° beamwidth (azimuth and elevation), 0° elevation pointing angle, 3.0-μs pulse width, and 120-ft antenna height. Although the S-band radar has a relatively strong output power, clutter data were recorded by a data collector having a limited dynamic range. To cover the full measurement range required for our tests, data were sequentially collected with attenuation levels of 80, 60, 40, 20, and 0 dB and later merged for expanded dynamic range. In the data merging process, a 17-dB lower limit and a 37-dB upper limit were used at each attenuator setting to eliminate system noise and saturated data, respectively. The clutter-pulse-noise-to-noise [(C+N)/N] ratio of the merged data ranged from 17 to 117 dB. The process of data collection at the five attenuator settings consumed approximately 4–6 min. In the merged data file, each clutter measurement has been attributed to a fixed radar cell despite the fact that the ship speed was approximately 10 knots during the data collection period. This extended data collection process effectively creates a smearing effect. The data collector can acquire measurements over an extended azimuth and range sector. In these tests, the azimuth and range sectors were approximately 130° and 63 nmi, respectively. Considering the range resolution (0.24 nmi), azimuth resolution (1.6°), and attenuator settings (5), more than 10^5 measurements compose a single range/azimuth data set. Multiple data sets were transferred to tape for later analysis.

Atmospheric data were collected using an instrumented helicopter that measured temperature, pressure, and humidity versus height. The helicopter flew a series of sawtooth patterns from the ship over the water, thereby allowing a sequence of profiles to be constructed as a function of range from the ship. Atmospheric data were collected 10–15 nmi inland. These data were later processed to determine a series of profiles of refractivity index versus height. During data collection, measured refractivity did not deviate significantly from a standard atmosphere condition. As a general rule, however, propagation in marine or coastal environments can deviate significantly from standard atmosphere conditions, resulting in significant variations in terrain clutter as seen by a shipboard radar (see preceding discussion).

A Ku-band and an X-band radar were used to collect land clutter data in the Arabian Gulf in February and June 1995. The Ku-band radar parameters are vertical polarization, 63-ft antenna height, 1.6° azimuth beamwidth, 10° elevation beamwidth (pointing at 4.5°), and 200-ns pulse width. The Ku-band radar has relatively low power, and the full measurement range can be covered by the 40-dB dynamic range of the CDC without adding attenuation. The X-band radar parameters are horizontal polarization, 58-ft antenna height, 1.5° azimuth beamwidth, 4.7° elevation beamwidth (pointing at 2.3°), and 260-ns pulse. The X-band measurements (using a 64-pulse compression/uncompression mode) were collected by the same type of CDC without adding an attenuator.

Atmospheric data were not collected during the Ku-band radar measurements, but since the Ku-band radar was very close to land, the radar measurements would not be significantly affected by the atmospheric conditions. An assumption of a standard atmosphere is used in the simulation to be discussed. For the X-band radar measurements, refractivity profile D of Fig. 1 was measured approximately 8 h before the data were collected.

Comparison of Measurement and Model: Geographic Patterns

Figure 16 illustrates several features of measured and simulated reflectivity data. Figure 16a shows a terrain profile determined from the DTED database for a single azimuth direction (106.34°) with the ship positioned in southern California. The highlighted regions represent directly illuminated terrain, as determined with the ray-trace algorithm. The terrain profile shown is

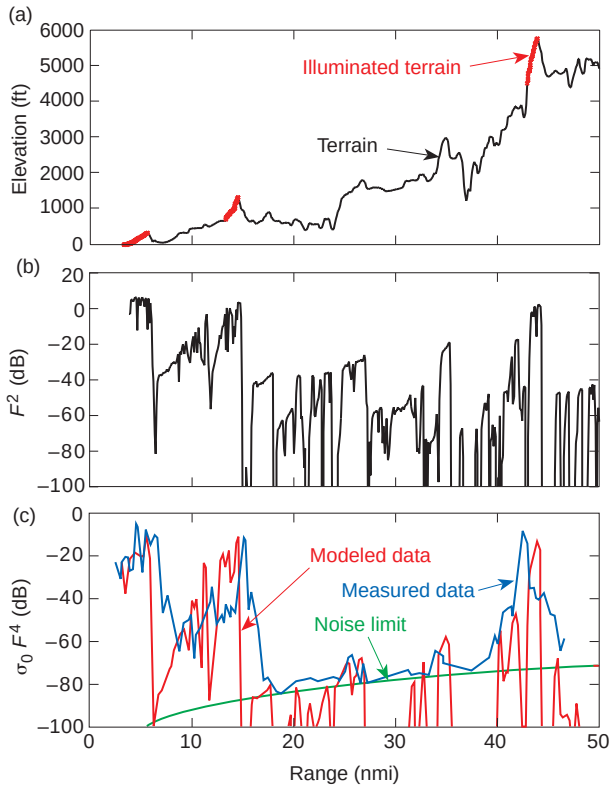

Figure 16. Simulated and measured land clutter reflectivity. (a) Terrain profile at radar beam center; (b) one-way propagation factor (F^2); (c) radar clutter reflectivity ($\sigma_0 F^4$).

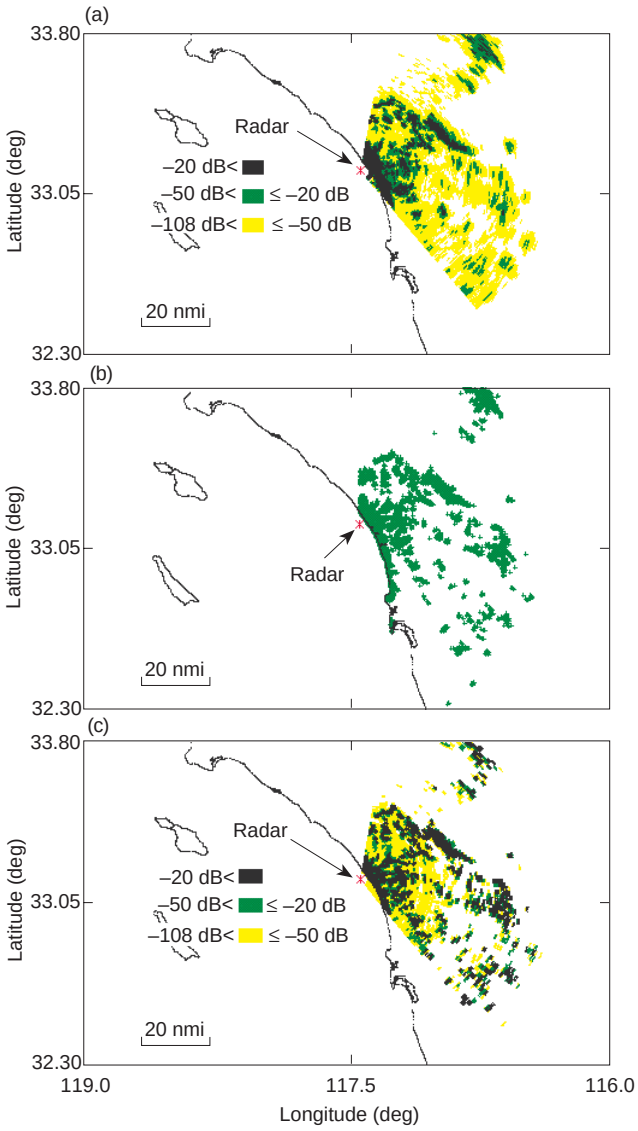

Figure 17. Comparison of land clutter measured and modeled data. (a) Measured radar clutter reflectivity ($\sigma_0 F^4$) at the coast of southern California within 63.0 nmi; (b) terrain visibility map predicted with the ray-trace method (standard atmosphere; antenna height = 120 ft); (c) map of simulated radar clutter reflectivity ($\sigma_0 F^4$) using RADSCAT method.

only one representation of the terrain contour within a radar beamwidth. Within a beamwidth, the terrain height will vary at a fixed range because of the azimuth extent of the beam, especially at the greater limits of range. Figure 16b shows the one-way propagation factor determined from the TEMPER program. Figure 16c shows measured and modeled values of $\sigma_0 F^4$ versus range, where the simulated data were obtained with the average of two azimuth slices per radar beamwidth. The magnitude of $\sigma_0 F^4$ necessary to equal system noise is also shown. As a general rule, measurements below the noise limit are not possible.

Figure 17a shows wide-area views of measured clutter in southern California. In Fig. 17a, magnitudes of $\sigma_0 F^4$ have been coded on a color scale; these magnitudes were derived from measurements of radar power using Eq. 1. This picture provides one example out of many such data sets collected during the exercise. Corresponding modeled data are shown in Figs. 17b and 17c. Figure 17b was derived from the Terrain Visibility Routine (TEVIR) using the ray-trace algorithm. Figure 17c was derived from the RADSCAT program.

By overlaying the measurement and simulation maps, one observes very good correspondence between the geographic patterns of measured and modeled data. The predicted areas of terrain illumination in the ray-trace routine (Fig. 17b) correspond well with the contours of measured clutter above –20 dB in Fig. 17a. This correspondence suggests that the strong clutter measurements are associated with directly illuminated terrain.

Figure 18 shows a terrain profile determined from the DTED database for a single azimuth direction (213.9°) and the corresponding measured data at Ku-band. The highlighted points on the terrain profile indicate directly illuminated terrain as determined by TEVIR. The positions of strong measured clutter returns coincide exactly at illuminated terrain shown in the figure. Figure 19 illustrates wide-area patterns of measured and simulated clutter. In Fig. 19a, magnitudes of measured (C+N)/N are color coded between

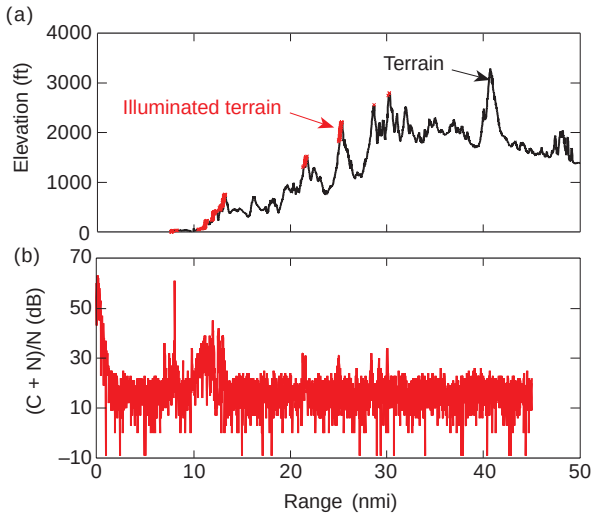

Figure 18. Land clutter return of Ku-band radar for a single azimuth direction (213.9°). (a) Terrain profile; (b) measured (C+N)/N (clutter-plus-noise-to-noise ratio).

193 to 247° in azimuth. By overlaying Figs. 19a and 19b, one finds good correspondence between the geographic patterns of measured data and simulated visible terrain, especially at close ranges. Because of the low power of the Ku-band radar, only the strongest clutter returns beyond 15 nmi can be represented. Consequently, the geographic size of measured land clutter is smaller than the simulated visible terrain at distant ranges.

Figure 20 illustrates several features of the measured and simulated clutter return, (C+N)/N, of an X-band (MK 92) radar. Figure 20a shows a terrain profile determined from the DTED database; Figs. 20b and 20c show the measured data without and with pulse compression, respectively. Figure 20d shows the simulated (C+N)/N of land clutter. The strongest measurements were seen to be saturated, as indicated by the flat tops in Fig. 20b. Since the pulse compression is a function of uncompressed pulse, the magnitude of the compressed data (Fig. 20c) is saturated as well. Despite the saturation of measured data, simulated data at all range positions agree with the patterns of illuminated terrain, which is highlighted in the terrain profile.

Figure 21a shows the terrain visibility map simulated by TEVIR near the coast of Iran under a strong surface-based duct. The beach area in the figure is directly illuminated due to the duct, but would not be illuminated under standard atmosphere propagation. Figure 21b shows the land clutter map of the X-band measurements with uncompressed pulse mode. Although the (C+N)/N data are saturated, they are adequate for a qualitative analysis. By comparing Figs. 21a and 21b, we observe good correspondence between the geographic patterns of measured data and simulated visible terrain.

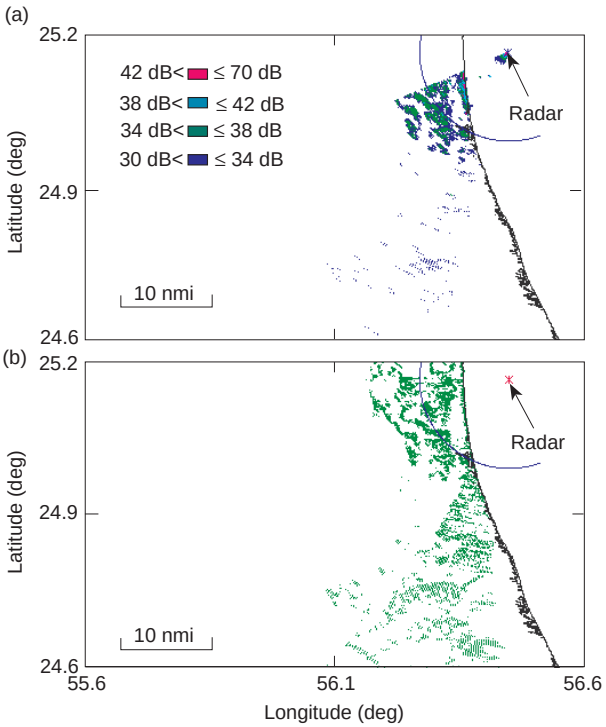

Figure 19. Comparison of measured data and simulated terrain visibility map. (a) Measured (C+N)/N (clutter-plus-noise-to-noise ratio) with Ku-band radar at the coast of United Arab Emirates; (b) simulated terrain visibility map predicted with TEVIR (standard atmosphere; antenna height = 63 ft).

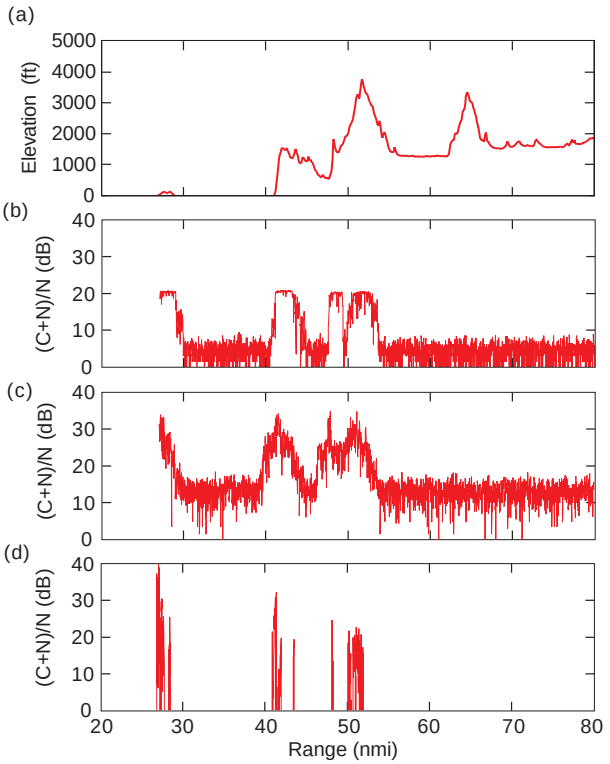

Figure 20. Land clutter return of an X-band radar. (a) Terrain profile; (b) uncompressed data; (c) compressed data; (d) simulated clutter.

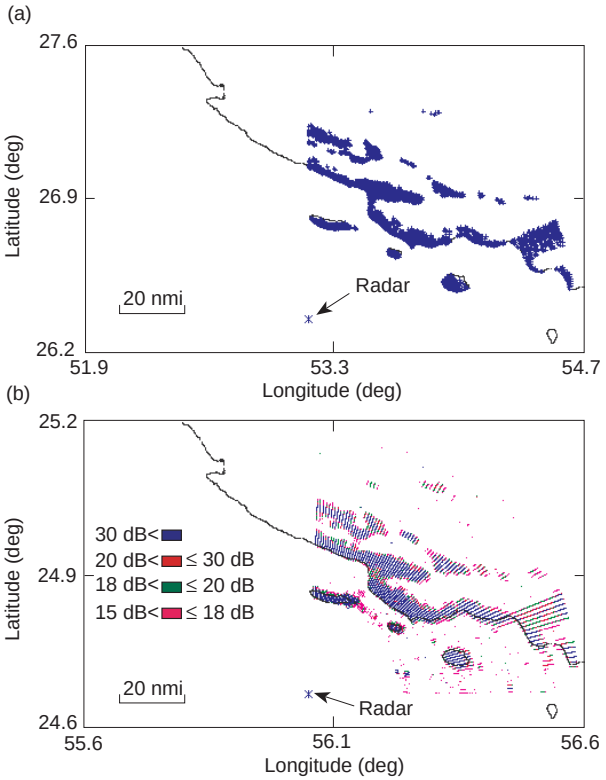

Figure 21. Comparison of simulated terrain visibility map and measured data. (a) Terrain visibility map predicted with TEVIR, at the coast of Iran (ducting atmosphere, antenna height = 58 ft); (b) measured (C+N)/N (clutter-plus-noise-to-noise ratio) collected with an X-band radar using 64-bit uncompressed pulse at the coast of Iran (data shown from 27 to 80 nmi in range and 0 to 90° in azimuth).

Statistical Representation

Figure 22 illustrates the cumulative distribution of measured and modeled reflectivity ($\sigma_0 F^4$) in southern California. The vertical axis gives the number of radar cells exceeding the value of $\sigma_0 F^4$ shown on the horizontal axis. One curve shows the measured data; the other lines show simulated data using the method described in the "Clutter Calculations" section with $\gamma = 0.17$. The modeled data includes calculated effects of various horizontal antenna sidelobe levels. Sidelobe effects were determined by integrating clutter from cells along a constant azimuth slice, but where the clutter magnitude was reduced by the assumed sidelobe level, and adding the integrated sidelobe clutter to the calculated main beam value. A sidelobe level of –80 dB approximates that of the experimental system.

For $\sigma_0 F^4$ greater than –40 dB, the measured and simulated results in Fig. 22 agree well. For weaker clutter, however, the model predictions are significantly below measurements. It was suspected that the lack of correspondence of weaker clutter might occur primarily in shadow (diffraction) regions. To test this hypothesis, we examined the distribution of measured and simulated clutter applying to radar cells that contained at least a portion of directly illuminated terrain as indicated by the ray-trace method. The resulting distributions are shown in Fig. 23. Two distributions are shown for the modeled data: one applies to the calculated values of $\sigma_0 F^4$, following the convention shown in Fig. 22; the other is obtained by random numbers drawn from a Raleigh power distribution, in which the mean value is defined by the calculated $\sigma_0 F^4$ for that cell. This distribution simulates a compound distribution as described previously. When statistical distributions are compared, the compound distribution is expected to most nearly simulate the measured data.

It is seen that the measured and modeled distributions in Fig. 23 correspond very well, suggesting that the model performs quite well when directly illuminated surfaces are contained within the radar cell. The median value of $\sigma_0 F^4$ is –23 dB for both measured and modeled data; the Weibull *a*-parameter is 1.7 for the measurements and the modeled compound distributions. These values compare favorably with previously published data at S-band.[1]

As indicated earlier, the X-band radar measurements were saturated as a result of the limited dynamic range of the CDC measurements. Therefore, further quantitative analysis is not possible using the X-band data. Figure 24 illustrates the cumulative distribution of

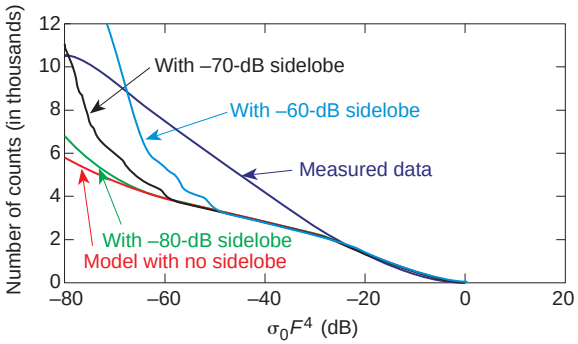

Figure 22. Cumulative distribution of radar clutter reflectivity ($\sigma_0 F^4$) for the coast of southern California; model with standard atmosphere, $\gamma = 0.174$, two-way sidelobe = –60 to –80 dB.

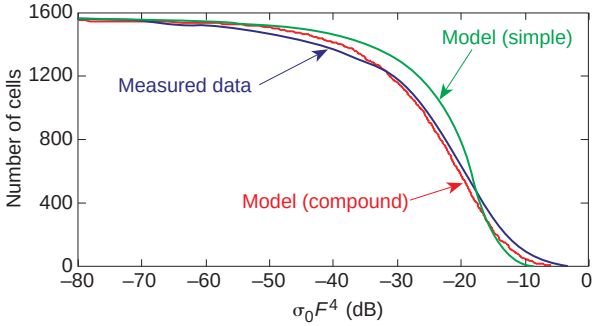

Figure 23. Cumulative distribution of radar clutter reflectivity ($\sigma_0 F^4$) applied to radar cells containing directly illuminated terrain for the coast of southern California.

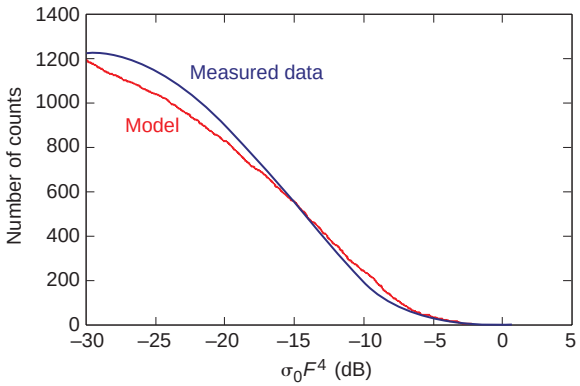

Figure 24. Cumulative distribution of radar clutter reflectivity ($\sigma_0 F^4$) applied to radar cells containing directly illuminated terrain for the coast of United Arab Emirates.

measured and modeled reflectivity of the Ku-band radar in the Arabian Gulf. As noted in Fig. 18b, the average value of (C+N)/N for the Ku-band data is 18 dB, which is higher than most clutter returns in the diffraction zone. For a valid comparison, in Fig. 24, the cumulative plot includes only the directly illuminated radar cells determinated by TEVIR. As with the X-band data, good correspondence between measured and modeled data is seen for strong returns. Unlike the S-band radar, no Ku-band data exist that can be used to validate the model for weak clutter. The simulated data in Fig. 24 were generated by the RADSCAT program, with $\gamma = 0.2$. According to Eq. 3, γ should equal 0.36 for a Ku-band radar. If the clutter model used $\gamma = 0.36$, the cumulative curve of the model would shift by 2 dB in Fig. 24. It would require further study to determine a correct γ relationship for different radar frequencies and terrain types.

Investigation of Differences Between Measurement and Model

The statistical distribution of measured and simulated clutter appears to correspond well for relatively strong clutter or for radar cells having directly illuminated surfaces. For weaker clutter or for clutter pertaining to shadow zones, the model appears to underpredict the measured S-band data. We are investigating several reasons for this discrepancy. The following describes potential sources of discrepancy that are being considered.

The sidelobes of an experimental system can increase the occurrence of relatively weak clutter. The S-band radar azimuth sidelobes, as seen in Fig. 22, do increase relatively weak clutter but not to an extent sufficient to bring the measurement and model in complete correspondence. The experimental S-band system also had elevation sidelobes and cross talk between vertically separated beams. The effects of these elevation sidelobes and cross talk were simulated and found to reduce the difference between measured and modeled data. We note that at the trailing edges of strong clutter peaks, the measured clutter tends to exceed the simulated data (see Fig. 16). The effects of vertical antenna beam cross talk appeared to account for the trailing edge effects. Despite this improvement, significant differences remained between measured and modeled data in the shadow zone ($\sigma_0 F^4$ below –40 dB).

The S-band data at five attenuator settings were collected over a period of 4–6 min, during which time the ship maintained a velocity of about 10 kt. To investigate the possible smearing effects of position changes during the data collection period, we need to simulate a database that contains such smearing effects.

As described in the section on visibility maps, terrain effects are incorporated into the TEMPER electromagnetic routine using an approximation to a perfectly absorbing boundary. We are considering the possibility that the terrain boundary method implemented in TEMPER might not adequately represent diffraction zone effects. Another simplification in the model is that the terrain boundary is two-dimensional, rather than three-dimensional, as in the real world. The use of a two-dimensional approximation will introduce errors into the simulation. Another possible source of error is that multiple scattering processes (as a result of the three-dimensional aspects of the terrain) are not included in the simulation.

SUMMARY

In this article, we discuss a model for terrain effects on shipboard radar performance that accounts for site-specific terrain features and for propagation effects. Both terrain shadowing and clutter can be simulated. The method can accommodate atmospheric data that vary in three dimensions, if such detailed information is available. Site-specific terrain contours are described through the DTED database, which is provided by the Defense Mapping Agency. The model is configured with various degrees of complexity. This article includes previously published results at the S-band[19] as well as more recent data at the X-band and Ku-band.

Relatively simple, but fast, methods are provided with TEVIR-I and -II. TEVIR-I computes terrain and target shadowing, where the propagation can be represented as straight-line propagation over a round Earth with an equivalent Earth radius factor. Atmospheric profiles fitting this category can be represented by a constant gradient of the index of refraction versus height. The "standard atmosphere" is one example fitting into this category. TEVIR-II also determines terrain and target shadowing, but with arbitrary atmospheric inputs.

The RADSCAT method employs an electromagnetic parabolic equation method to calculate the propagation

factor. RADSCAT includes both refraction and diffraction effects and can simulate terrain shadowing and backscatter. This method can accept refractivity that varies in three dimensions. Although the RADSCAT method provides much more detailed information, it also takes much more time to execute as compared with the TEVIR methods.

Variations in atmospheric refractivity can significantly alter patterns of terrain clutter and shadowing. The effects will depend on the structure of atmospheric refractivity as well as terrain relief. With a surface-based duct, for instance, it is possible to markedly increase the density of directly illuminated terrain or to greatly extend the range extent over which strong clutter is returned.

The RADSCAT and TEVIR models were compared with radar measurements taken off the west coast of the United States from an S-band radar. The correspondence between measured and simulated clutter is very good for relatively strong clutter. This correspondence is evident in the geographic patterns and statistical distribution of clutter returns in both northern Washington and southern California. Although the terrain has similar mountainous relief in the two locations, the composition of the terrain is quite different. In the measurement area of northern Washington, the terrain is forested, with little cultural development. In southern California, the terrain is semiarid with significant cultural development, particularly along the coast. Despite the differences in terrain composition, the clutter returns on directly illuminated surfaces were similar in the two locations.

Other data used in this study were collected by Ku-band radar under the standard atmosphere condition near the west coast of the United Arab Emirates and by X-band under a strong surface-based duct near the coast of Iran. In both cases, excellent agreement between measurements and modeled clutter was obtained when the spatial patterns of strong clutter returns were compared.

Within shadowed regions, the model predicts generally lower clutter strengths as compared with measurements. We are currently investigating several hypotheses that might explain the discrepancy. Primary considerations include smearing due to platform motion during the measurement interval, inadequate representation of diffraction, multiple scattering effects, data collection response dynamics, and refractive effects of vegetation.

Future improvements in the model will incorporate the Digital Feature Analysis Data (DFAD) database of terrain composition. This database, also published by the Defense Mapping Agency, indicates features such as vegetation, structures, roads, bridges, and power lines. With such data, it is possible to better predict backscatter and the effects of both natural and cultural features.

REFERENCES

1. Nathanson, F. E., Reilly, J. P., and Cohen, M. N., *Radar Design Principles*, 2nd Ed., McGraw-Hill, Inc., New York (1991).
2. Long, M. W., *Radar Reflectivity of Land and Sea*, Artech House, Dedham, MA (1983).
3. Ulaby, F. T., and Dobson, M. C., *Handbook of Radar Scattering Statistics for Terrain*, Artech House, Norwood, MA (1989).
4. Barton, D. K., "Land Clutter Models for Radar Design and Analysis," *Proc. IEEE* **73**(2), 198–204 (1985).
5. Henn, J. W., Pictor, D. H., and Webb, A., "Land Clutter Study: Low Grazing Angles (Backscattering)," in *Advances in Radar Techniques*, J. Clark (ed.), Peter Peregrines Ltd., London, England, pp. 222–226 (1985).
6. Currie, N. C., and Zehner, S. P., "Millimeter Wave Land Clutter Model," in *Advances in Radar Techniques*, J. Clarke (ed.), Peter Peregrines Ltd., London, England, pp. 227–231 (1985).
7. Billingsley, J. B., "Radar Ground Clutter Measurements and Models, Part I: Spatial Amplitude Statistics," *AGARD Conference Proceedings on Target & Clutter Scattering and Their Effects on Military Radar Performance*, AGARD-CP-501, NATO Electromagnetic Wave Propagation Panel Meeting, Ottawa, Canada, DTIC No. AD-P006373, pp. 1.1–1.15 (May 1994).
8. Ayasli, S., "SEKE: A Computer Model for Low Altitude Radar Propagation Over Irregular Terrain," *IEEE Trans. Ant. Prop.* **AP-34**(8), 1013–1023 (1986).
9. Dockery, G. D., "Modeling Electromagnetic Wave Propagation in the Troposphere Using the Parabolic Equation," *IEEE Trans. Ant. Prop.* **36**(10), 1464–1470 (1988).
10. Kuttler, J. R., and Dockery, G. D., "Theoretical Description of the Parabolic Approximation: Fourier Split-Step Method of Representing Electromagnetic Propagation in the Troposphere," *Radio Sci.* **26**(2), 381–393 (1991).
11. Reilly, J. P., Lin, C. C., and Rudie, S. A., "Land Clutter and Shadowing With Consideration of Propagation in Coastal Regions," *Proc. Radar '92*, Brighton, England, pp. 26–29 (Oct 1992).
12. Paulus, R. A., "Practical Applications of an Evaporative Duct Model," *Radio Sci.* **20**(4), 887–896 (1985).
13. Lin, C. C., and Reilly, J. P., "Radar Terrain Clutter Model with Consideration of Propagation Effects," *Proc. 23rd European Microwave Conf.*, Madrid, Spain, pp. 478–482 (Sep 1993).
14. Marcus, S. W., "A Hybrid (Finite Difference–Surface Green's Function) Method for Computing Transmission Losses in an Inhomogeneous Atmosphere Over Irregular Terrain," *IEEE Trans. Ant. Prop.* **40**(12), 1451–1458 (1992).
15. Levy, M. F., "Parabolic Equation Modeling of Propagation Over Irregular Terrain," *Electron. Lett.*, **26**(15), 1153–1155 (1990).
16. Beckman, P., "Scattering by Composite Rough Surfaces," *Proc. IEEE* **53**, 1012–1015 (Aug 1965).
17. Barrick, D. E., "Rough Surface Scattering Based on the Specular Point Theory," *IEEE Trans. Ant. Prop.* **AP-16**(4), 449–454 (July 1968).
18. Beckman, P., and Spizzochino, A., *The Scattering of Electromagnetic Waves from Rough Surfaces*, Artech House, Norwood, MA (1987).
19. Reilly, J. P., and Lin, C. C., "A Propagation-Based Model of Terrain Effects for Shipboard Radar Applications," *Proc. NATO AGARD-SPP Meeting*, Bremerhaven, Germany (Sep 1994).

ACKNOWLEDGMENTS: This work has been supported through the U.S. Navy Aegis Shipbuilding Program, PMS-400.

THE AUTHORS

CHRISTOPHER C. LIN received his B.S. and M.S. degrees in electrical engineering from Drexel University in 1983 and 1985, respectively. He joined APL in 1985 and is a Senior Staff engineer in the Sensor Signal and Data Processing Group of the Air Defense Systems Department. He has worked on a variety of projects for radar detection and tracking systems, and developed the algorithm for multisensor tracking. Currently, Mr. Lin is developing a terrain effects clutter model for shipboard radar applications. His e-mail address is Chris.Lin@jhuapl.edu.

J. PATRICK REILLY is a member of APL's Principal Professional Staff and supervisor of the Environmental Modeling Section of the Sensor Signal and Data Processing Group in the Air Defense Systems Department. He obtained a B.E.E. from the University of Detroit in 1962 and an M.S.E. from George Washington University in 1965. Since joining APL in 1962, he has worked on a variety of theoretical and experimental projects associated with radar, sonar, acoustics, infrared systems, and bioelectric phenomena. He supervised the Electromagnetics and Acoustics Section of the Environmental Assessment Group, and was the director of research programs on human reactions to electric currents and electromagnetic fields. Mr. Reilly is a senior member of the IEEE and a member of the Bioelectromagnetics Society. He is the author of a book entitled *Electrical Stimulation and Electropathology*, and also the co-author of another book entitled *Radar Design Principles*. His e-mail address is Patrick.Reilly@jhuapl.edu.